Effect of Ga and Cd substitutions on the first-order antiferromagnetic transition in NdCo$_2$Zn$_{20}$

Rikako Yamamoto [1], Reiji J. Yamada,[1] Yu Yamane [1], Yasuyuki Shimura,[1] Kazunori Umeo,[2]
Toshiro Takabatake,[1] and Takahiro Onimaru [1,*]

[1]*Department of Quantum Matter, Graduate School of Advanced Science and Engineering, Hiroshima University,
Higashi-Hiroshima, Hiroshima 739-8530, Japan*
[2]*Department of Low Temperature Experiment, Integrated Experimental Support/Research Division, Natural Science Center for Basic
Research and Development (N-BARD), Hiroshima University, Higashi-Hiroshima, Hiroshima 739-8526, Japan*

The cubic neodymium-based compound NdCo$_2$Zn$_{20}$ exhibits a first-order antiferromagnetic (AFM) transition at $T_N = 0.53$ K. Strong magnetic fluctuations at temperatures up to 5 K were suggested by the downward curvature of the electrical resistivity $\rho(T)$ and the reduced magnetic entropy S_m of $0.5R\ln2$ at T_N. In this study, we measured $\rho(T)$, the isothermal magnetization $M(B)$, magnetic susceptibility $\chi(T)$, and specific heat $C(T)$ of NdCo$_2$Zn$_{20-x}$Cd$_x$ for $x = 1$ and NdCo$_2$Zn$_{20-y}$Ga$_y$ for $y = 1$ and 2. The sharp peak of the magnetic specific heat $C_m(T)$ at T_N for $x = 0$ is changed to a weak and broad maximum at 0.55 K for $x = 1$. This drastic change in $C_m(T)$ suggests that the isovalent Cd substitution for Zn disorders the exchange interactions between the Nd moments to hinder the first-order AFM transition. On the other hand, $C_m(T)$ for $y = 1$ and 2 exhibits a lambda-shaped anomaly, which is a characteristic of a second-order AFM transition, at elevated temperatures of 0.78 and 1.5 K, respectively. The stabilization of the AFM order by the Ga substitution indicates that $4p$ electron doping strengthens the AFM interaction. We therefore propose that the first-order transition in NdCo$_2$Zn$_{20}$ is maintained by competitive magnetic interactions inherent in the Nd diamond sublattice.

I. INTRODUCTION

A series of compounds RTr_2X_{20} (R: rare-earth, Tr: transition metal, X = Al, Zn, and Cd) exhibits a variety of strongly correlated electronic phenomena owing to characteristics of the cubic CeCr$_2$Al$_{20}$-type crystal structure with the space group of $Fd\bar{3}m$ (No. 227, O_h^7) [1]. The sublattices of the R and Tr atoms at the 8a and 16d sites, respectively, are identical to the diamond and pyrochlore lattices. In addition, since the R ion is encapsulated in a highly symmetric Frank-Kasper cage formed by 16 X atoms, the crystalline electric field (CEF) becomes weak while hybridization of the $4f$ electrons with the conduction electrons (c–f hybridization) is strengthened. In fact, the combination of the weak CEF effect with the strong c–f hybridization gives rise to interesting correlated electronic phenomena such as a heavy fermion state in YbCo$_2$Zn$_{20}$ with $4f^{13}$ configuration having an extremely large electronic specific heat coefficient of $\gamma = 8$ J/K^2 mol [2–4], the coexistence of superconductivity and quadrupole order in $4f^2$ systems of PrTr_2Zn$_{20}$ (Tr = Rh, Ir) and PrTr_2Al$_{20}$ (Tr = V, Ti) with non-Kramers doublet ground states [5–10], and non-Fermi liquid (NFL) behaviors owing to the formation of the two-channel Kondo lattice in PrTr_2Zn$_{20}$ (Tr = Rh, Ir) [11–13]. Concerning the NFL behaviors in PrIr$_2$Zn$_{20}$, the characteristic temperature determined from the downward curvature of the electrical resistivity $\rho(T)$ decreases with the Cd substitution for Zn but increases with the Ga substitution

[14]. This trend indicates that the quadrupole Kondo lattice is stabilized owing to the strengthening of the c–f hybridization by the chemical pressure and the enhanced density of states of the conduction electrons. Furthermore, single-site NFL behaviors of $\rho(T)$ and specific heat observed in a diluted Pr system Y$_{1-x}$Pr$_x$Ir$_2$Zn$_{20}$ suggest the manifestation of the single-site two-channel Kondo effect [15–17].

On the other hand, the isostructural Nd-based compounds with $4f^3$ configuration exhibit ferromagnetic (FM) or antiferromagnetic (AFM) phase transitions. The magnetic orders are caused by exchange interactions between the magnetic dipoles in the CEF ground states of the Nd^{3+} ion, which are mostly the Kramers Γ_6 doublets [18–25]. Among them, NdCo$_2$Zn$_{20}$ undergoes an AFM order at $T_N = 0.53$ K, in which only $4f$ electrons are involved [22]. Note that the lattice parameter of NdCo$_2$Zn$_{20}$ is the smallest among the NdTr_2X_{20} compounds (X = Al and Zn). An extremely sharp peak of the specific heat C and an abrupt drop of the magnetic susceptibility $\chi(T)$ at $T < T_N$ suggest a first-order phase transition. It was corroborated by observation of the hysteretic temperature variation of the thermal expansion [26]. In contrast, for the isostructural NdTr_2Zn$_{20}$ (Tr = Ru, Os, Rh, and Ir), anomalies of the magnetic specific heat C_m are lambda-type shapes, which are characteristics of second-order magnetic transitions [18–23].

Moreover, in NdCo$_2$Zn$_{20}$, peculiar behaviors of the physical quantities were observed in the paramagnetic state above T_N. The electrical resistivity $\rho(T)$ shows a downward curvature on cooling from 5 K to $T_N = 0.53$ K. In addition, the magnetic entropy S_m at T_N is 50% of $R\ln2$ (R is the gas

*onimaru@hiroshima-u.ac.jp

TABLE I. Lattice parameters a (Å), residual resistivity ratio RRR $= \rho(300\,\mathrm{K})/\rho(3\,\mathrm{K})$, effective magnetic moments μ_{eff} (μ_B / Nd), paramagnetic Curie temperatures θ_{p} (K), and $\theta_{\mathrm{p}}^{\mathrm{low}}$ (K), respectively, evaluated from the $\chi^{-1}(T)$ data for $50 < T < 300$ K and $T < 7$ K, intersite magnetic interactions K (K), and magnetic transition temperatures T_{N} (K) of NdCo$_2$Zn$_{20}$ [22], NdCo$_2$Zn$_{20-x}$Cd$_x$ for $x = 1$, and NdCo$_2$Zn$_{20-y}$Ga$_y$ for $y = 1$ and 2.

	a (Å)	RRR	μ_{eff} (μ_B / Nd)	θ_{p} (K)	$\theta_{\mathrm{p}}^{\mathrm{low}}$ (K)	K (K)	T_{N} (K)
$x = 1$	14.1652(4)	14	3.93	-7.9	0.33	0.25	0.55
$x, y = 0$	14.110(1)	8.3	3.90	-7.1	0.10	0.22	0.53
$y = 1$	14.1115(6)	2.6	3.80	-11	-1.01	-0.10	0.78
$y = 2$	14.1260(12)	3.3	3.61	-2.3	-3.21	-0.40	1.50

constant). The full recovery to $R\ln 2$, which is expected for the Γ_6 doublet ground state, is achieved on heating to 5 K. The downward curvature of $\rho(T)$ and the reduced S_{m} at T_{N} imply that strong magnetic fluctuations exist in the range of $T_{\mathrm{N}} < T < 5$ K, which may be relevant to the first-order transition. There are two possible origins of the magnetic fluctuations above T_{N}. One is the formation of a two-channel Kondo lattice. In fact, the downward variation of $\rho(T)$ can be reproduced by calculation using the two-channel Anderson lattice model [13]. Hotta predicted that Nd-based intermetallic compounds with the Γ_6 doublet ground state are candidates exhibiting the two-channel Kondo effect, allowing the residual entropy of $0.5R\ln 2$ [27]. Another is the magnetic frustration inherent in the diamond lattice due to competitive nearest- and next-nearest-neighbor exchange interactions [28,29]. NdCo$_2$Zn$_{20}$ having the Nd diamond sublattice shows the AFM transition, above which FM interaction is needed to reproduce the magnetic susceptibility with a positive paramagnetic Curie temperature [22]. Thereby, competitive magnetic correlations due to the magnetic frustration could lift the degeneracy of the Γ_6 doublet at $T_{\mathrm{N}} < T < 5$ K.

Substitution of NdCo$_2$Zn$_{20}$ was so far reported on NdCo$_2$Zn$_{18}$Sn$_2$ [30]. A negative chemical pressure was expected because the lattice parameter of $a = 14.2832$ Å is larger than that of NdCo$_2$Zn$_{20}$ [22]. In fact, the overall energy of CEF splitting is reduced to less than a half that of NdCo$_2$Zn$_{20}$. The specific heat shows a steep decrease at 1.0 K, indicating a magnetic phase transition.

In this paper, we studied the effect of Cd and Ga substitutions for Zn on the first-order AFM transition in NdCo$_2$Zn$_{20}$. In particular, we examined how the downward curvature of $\rho(T)$ is modified and whether the reduced S_{m} is recovered by the substitution. We measured $\rho(T)$, $\chi(T)$, isothermal magnetization $M(B)$, and $C(T)$ of NdCo$_2$Zn$_{20-x}$Cd$_x$ for $x = 1$ and NdCo$_2$Zn$_{20-y}$Ga$_y$ for $y = 1$ and 2. Because the ionic radius of Cd^{2+} (Ga^{3+}) is larger (smaller) than that of Zn^{2+}, the cubic lattice parameter is supposed to increase (decrease) by increasing x (y). Moreover, given that the number of $4p$ electrons donated from Ga^{3+} ions is one more than that from Zn^{2+} ions, the $4p$ electronic density of state is increased to strengthen the c–f hybridization with increasing y. As described above, the characteristic temperature of the NFL behaviors in the non-Kramers system PrIr$_2$Zn$_{20}$ is largely changed by the Cd and Ga substitutions [14]. Likewise, the effect of the Cd and Ga substitutions on the transport and magnetic properties of NdCo$_2$Zn$_{20}$ should give a clue to understanding how the first-order AFM transition is related to

the release of $S_{\mathrm{m}}(T)$ and the downward curvature of $\rho(T)$ at $T > T_{\mathrm{N}}$.

II. EXPERIMENTAL PROCEDURE

Polycrystalline samples of NdCo$_2$Zn$_{20-x}$Cd$_x$ for $x = 1$ and NdCo$_2$Zn$_{20-y}$Ga$_y$ for $y = 1$ and 2 were synthesized by the vertical Bridgman method in a tube furnace with a siliconit heater. High purity elements of Nd (99.9%), Co (99.9%), Zn (99.9999%), Cd (99.999%), and Ga (99.9999%) were used. The initial concentrations of elements are Nd : Co : Zn : (Cd/Ga) $= 1.05 : 2 : 20 - (x/y) : (x/y)$. The constituent elements were placed in a quartz ample coated with carbon. The quartz ample was sealed under approximately 1/3 atmospheric pressure of high purity Ar. The elements were melted together at 950°C for 33 hours, and then the ample was brought down slowly at a speed of 2 mm/h.

The powder x-ray diffraction analysis of the samples confirmed the cubic CeCr$_2$Al$_{20}$-type crystal structures [1]. The lattice parameters a were determined by the Rietveld refinement using a program RIETAN-FP [31]. As listed in Table I, a for $x = 1$ is 0.38% larger than that for $x = 0$ [22], whereas the a parameters for $y = 1$ and 2 are comparable with that of $y = 0$. The real values of x and y were determined by the wavelength dispersive electron-probe micro-analysis with an electron beam of 20 keV using a JEOL JXA-8200 analyzer. By averaging the data of ten spots, x and y were determined as 0.95(3) for $x = 1$, 0.97(4) and 1.94(5) for $y = 1$ and 2, respectively. For simplicity, we will describe the concentration as $x = 1$, $y = 1$ and 2 hereafter. The electron-probe micro-analysis detected small amounts of impurities, which volume fractions are less than 1% of the whole region. Because of the small fractions, no additional peaks were observed in the x-ray powder diffraction patterns. The back-scattered electron images and the x-ray powder diffraction patterns are shown in the Supplementary Materials [32].

The electrical resistance was measured by a standard four-probe AC method with laboratory-built systems using a Gifford-McMahon-type refrigerator in the temperature range of 3–300 K and a commercial Cambridge Magnetic Refrigerator mFridge for 0.04–5 K. The dimensions of the samples for the resistance measurements are 0.066–0.167 mm^2 cross section and 1.0–1.9-mm length, and the distances between terminals for the voltage measurements are 0.58–0.98 mm. Magnetization was measured from 1.8 to 300 K in magnetic fields up to 5 T using a commercial superconducting quantum interference device magnetometer (MPMS, Quantum Design). To perform magnetization measurements at low
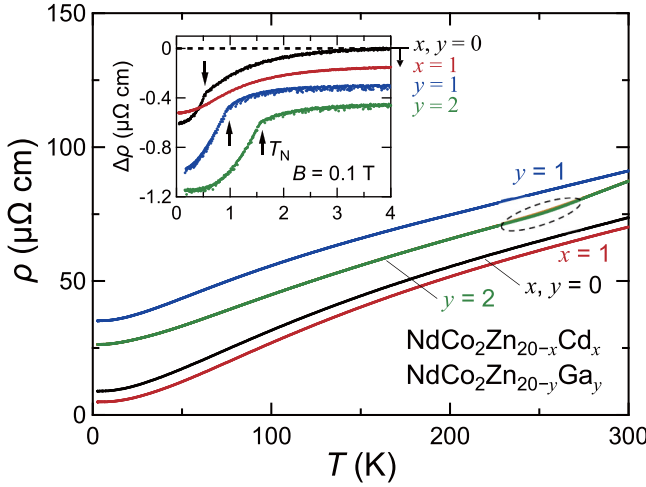
FIG. 1. Electrical resistivity ρ versus temperature of NdCo$_2$Zn$_{20}$ [22], NdCo$_2$Zn$_{20-x}$Cd$_x$ for $x = 1$ and NdCo$_2$Zn$_{20-y}$Ga$_y$ for $y = 1$ and 2. The inset shows the difference of $\rho(T)$ from the value at 4 K, $\Delta\rho(T) = \rho(T) - \rho(4\,\text{K})$. The data of $x = 1, y = 1$ and 2 are offset for clarity. A magnetic field of $B = 0.1$ T was applied to kill extrinsic superconductivity of impurity phases.

FIG. 2. Temperature dependence of the inverse magnetic susceptibility χ^{-1} of NdCo$_2$Zn$_{20}$ [22], NdCo$_2$Zn$_{20-x}$Cd$_x$ for $x = 1$, and NdCo$_2$Zn$_{20-y}$Ga$_y$ for $y = 1$ and 2 measured at $B = 0.1$ T. The upper inset shows the magnetic specific heat divided by temperature, C_m/T, versus T. The solid line represents the CEF calculation using the parameters of $W = 0.85$ K and $X = -0.285$ determined for NdCo$_2$Zn$_{20}$ [22]. The CEF level scheme of the Nd ion is depicted. The lower inset shows the $\chi^{-1}(T)$ data for $T \leqslant 20$ K.

temperatures down to 0.25 K, we adopted a capacitive Faraday method using a high-resolution capacitive force-sensing device installed in a ^{3}He single-shot refrigerator (Heliox, Oxford Instruments) [33]. Heat capacity measurements were conducted by the thermal relaxation method between 0.37 and 300 K in magnetic fields up to 4 T using a physical property measurement system (PPMS, Quantum Design).

III. RESULTS AND DISCUSSION

Temperature dependencies of $\rho(T)$ of NdCo$_2$Zn$_{20}$ [22], NdCo$_2$Zn$_{20-x}$Cd$_x$ for $x = 1$ and NdCo$_2$Zn$_{20-y}$Ga$_y$ for $y = 1$ and 2 are shown in Fig. 1. The $\rho(T)$ data for all the samples decrease on cooling from 300 K to 3 K. As shown in Table I, the residual resistivity ratio defined as RRR = $\rho(300\,\text{K})/\rho(3\,\text{K})$ is 14 for $x = 1$, which is higher than 8.3 for $x = 0$. On the other hand, the values of 2.6 and 3.3 for $y = 1$ and 2, respectively, are much lower than that for $y = 0$.

In Fig. 1, the $\rho(T)$ data for $y = 2$ exhibit a small hysteresis between 230 and 270 K in the region enclosed by the dashed oval, probably due to a structural transition, whereas no hysteresis was observed in the samples for $x, y = 0, x = 1$, and $y = 1$. However, no clear anomaly was observed in the $C(T)$ measurement. We remember that a similar hysteresis in $\rho(T)$ was observed between 170 and 470 K for an isostructural compound PrRh$_2$Zn$_{20}$, where no anomaly was found in the $C(T)$ measurement [34]. The inelastic neutron scattering measurements suggest that the local symmetry of the Pr ion sites changes from cubic T_d ($\bar{4}3m$) to cubic T (23) [35]. Because the transition is associated with only small displacements of Zn atoms at the 96g site, the entropy change is too small to be detected in the specific heat measurements. More obvious bends in $\rho(T)$ due to structural transitions were reported in some isostructural compounds such as RRu$_2$Zn$_{20}$ (R = La and Pr) [5,36–38] and ROs$_2$Zn$_{20}$ (R = La, Ce, Pr, and Nd) [20]. Superlattice reflections detected below the transition

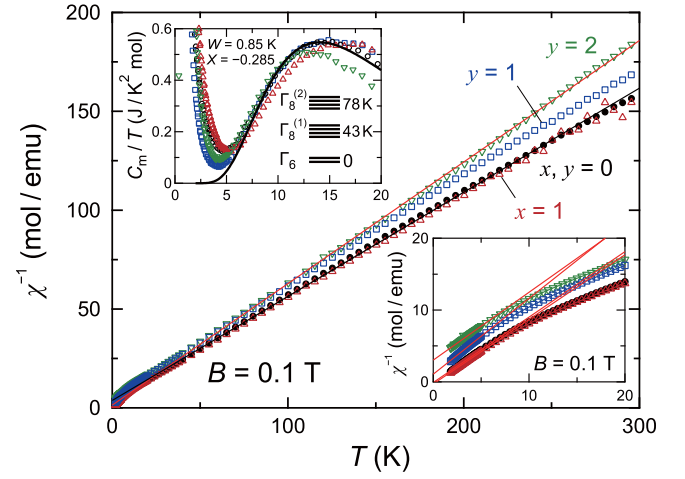temperatures in RRu$_2$Zn$_{20}$ (R = La and Pr) indicate symmetry lowering of the cubic structure [5,39], where low-energy optical phonon modes of the Zn atoms of the 16c site at 3 meV play a role in the structural instability [36–38]. Therefore, the hysteresis of $\rho(T)$ for $y = 2$ probably results from structural instability similar to that in PrRh$_2$Zn$_{20}$ [40].

The inset of Fig. 1 shows $\Delta\rho(T) = \rho(T) - \rho(4\,\text{K})$. The $\Delta\rho(T)$ data of $x = 1, y = 1$ and 2 are vertically shifted in the order from the base line. For $x = 1$ (red), any bend does not appear down to 0.05 K. The downward curvature of $\rho(T)$ for $T < 4$ K could be understood by the two-channel Anderson lattice model explained above [13,22]. However, since the c–f hybridization may be weakened by the Cd substitution due to the negative chemical pressure, the two-channel Kondo effect is unlikely as the origin of the downward variation of $\rho(T)$. In contrast, for $x, y = 0, y = 1$ (blue), and 2 (green), the $\Delta\rho(T)$ data bend at 0.53, 0.98, and 1.6 K, respectively, which result from the AFM transitions as will be described later.

Figure 2 shows the inverse magnetic susceptibility $\chi^{-1}(T)$ measured at $B = 0.1$ T between 1.8 and 300 K. The Curie–Weiss fits to the data between 50 and 300 K yield the paramagnetic Curie temperatures of θ_p and the effective magnetic moments of μ_{eff} the values of which are listed in Table I. The values of μ_{eff} for all the samples are close to 3.62 μ_B for a free Nd^{3+} ion. $\chi^{-1}(T)$ deviates from the Curie–Weiss behavior at $T < 10$ K as a result of the CEF effect as mentioned in the previous report on NdCo$_2$Zn$_{20}$ [22]. The $\chi^{-1}(T)$ data for $T \leqslant 20$ K are replotted in the lower inset of Fig. 2. The linear fits to the data below 7 K yield $\theta_p^{\text{low}} = +0.10$ K for $x, y = 0, +0.33$ K for $x = 1$, and -1.01 and -3.21 K for $y = 1$ and 2, respectively. The positive and negative signs of θ_p^{low} are consistent with the ferro- and antiferro-type magnetic interactions, respectively, evaluated from the isothermal magnetization data as will be shown later.
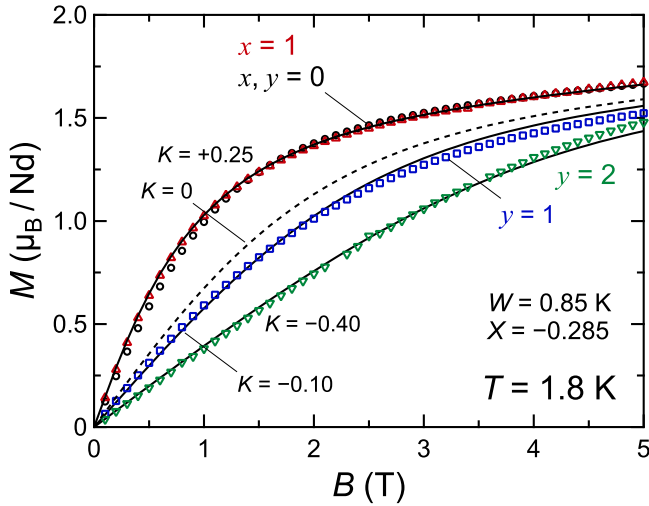
FIG. 3. Isothermal magnetization $M(B)$ at 1.8 K of NdCo$_2$Zn$_{20}$ [22], NdCo$_2$Zn$_{20-x}$Cd$_x$ for $x = 1$, and NdCo$_2$Zn$_{20-y}$Ga$_y$ for $y = 1$ and 2. The dashed line is the calculation using the CEF parameters of W = 0.85 K and $X = -0.285$, which describes the Γ_6 doublet ground state, without intersite magnetic interaction, $K = 0$. The solid lines are the calculations including the intersite magnetic interactions of K = +0.25 K for $x = 1$, -0.10 K for $y = 1$, and -0.40 K for $y = 2$.

FIG. 4. Temperature dependence of the magnetic specific heat divided by temperature, C_m/T, of NdCo$_2$Zn$_{20}$, NdCo$_2$Zn$_{20-x}$Cd$_x$ for $x = 1$ and NdCo$_2$Zn$_{20-y}$Ga$_y$ for $y = 1$ and 2. The arrows denote the AFM transition temperatures T_N. Inset: Magnetic entropy S_m estimated by integrating the C_m/T data with respect to the temperature. The S_m data are vertically lifted to reach the value of $R\ln2$ at 5 K. The C_m and S_m data for $x, y = 0$ are cited from [22].

The magnetic specific heat divided by temperature, C_m/T, is plotted versus T in the upper inset of Fig. 2. We evaluated C_m by subtracting the specific heat of a nonmagnetic counterpart YCo$_2$Zn$_{20}$ as the lattice contribution from the measured specific heat. At around 13 K, pronounced maxima exist in all the data, which can be reproduced by the CEF calculation as described below. Under the cubic CEF, the tenfold multiplet of $J = 9/2$ of the Nd^{3+} ion splits into a Γ_6 doublet and two Γ_8 quartets [41]. As shown with the solid line, the data of C_m/T can be well fitted by the CEF scheme with the Γ_6 doublet ground state and the excited $\Gamma_8^{(1)}$ and $\Gamma_8^{(2)}$ quartets at 43 K and 78 K, respectively. Here, we used the CEF parameters of $W = 0.85$ K and $X = -0.285$ which were chosen for NdCo$_2$Zn$_{20}$ [22]. It is worth noting that the CEF parameters and thus the level scheme are not affected by the Cd and Ga substitutions. This is in contrast to the case of NdCo$_2$Zn$_{18}$Sn$_2$, where the CEF splitting energy is reduced to one-half that of NdCo$_2$Zn$_{20}$ [30].

Isothermal magnetization $M(B)$ data at 1.8 K are plotted in Fig. 3. The $M(B)$ curve for $x = 1$ almost agrees with that of $x = 0$. In contrast, the curvature of $M(B)$ is suppressed successively with increasing y to 1 and 2. The suppressed curvature of $M(B)$ suggests the enhancement of AFM interaction by the Ga substitution, which is attributed to the effect of $4p$ electron doping. We reproduce the $M(B)$ data by the calculation with the above CEF parameters including the intersite magnetic interaction between the Nd magnetic moments. Here, we use the mean-field Hamiltonian including CEF Hamiltonian $\mathcal{H}_{CEF}$,

$$\mathcal{H} = \mathcal{H}_{CEF} + g_J\mu_B\boldsymbol{J}\boldsymbol{B} - K\langle\boldsymbol{J}\rangle\boldsymbol{J}, \quad (1)$$

where $g_J = 8/11$ is the Landé g-factor for a Nd^{3+} ion, J the total angular momentum, and K a coefficient expressing the intersite magnetic interaction between the Nd moments. $\mathcal{H}_{CEF}$
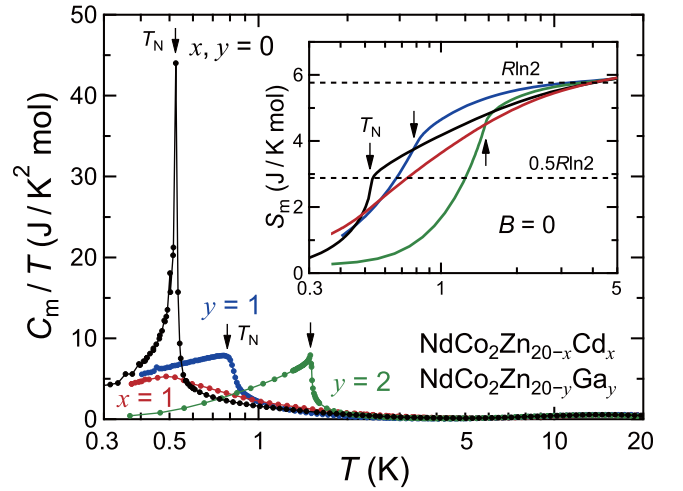
for the Nd^{3+} ion under the cubic CEF is described as [41]

$$\mathcal{H}_{CEF} = W\left[\frac{X}{60}(O_4^0 + 5O_4^4) + \frac{1 - |X|}{2520}(O_6^0 - 21O_6^4)\right], \quad (2)$$

where O_n^m are the Stevens operators [42]. The dashed line in Fig. 3 is the calculation using the above CEF parameters of $W = 0.85$ K and $X = -0.285$ without intersite magnetic interaction, $K = 0$. It dose not reproduce the experimental data at all. Calculations including the intersite magnetic interaction are shown with the solid lines. For $x = 1$, the calculation with the ferromagnetic interaction of $K = +0.25$ K reproduces the data. The data for $y = 1$ and 2, on the other hand, can be fitted by using negative $K = -0.10$ and -0.40 K. As shown in Table I, the positive and negative signs of K for the Cd and Ga substituted samples, respectively, are consistent with those of θ_p^{low}.

Figure 4 shows the temperature variation of C_m/T. The sharp peak at 0.53 K for $x = 0$, which is the hallmark of the first-order transition, is suppressed and changed to a broad maximum at 0.55 K for $x = 1$. For $y = 1$ and 2, on the other hand, lambda-shaped anomalies appear at $T_N = 0.78$ and 1.50 K, respectively, where the $\rho(T)$ data bend as shown with the arrows in the inset of Fig. 1. The increase in T_N with increasing y is consistent with the development of the AFM interaction as indicated by the suppression of the curvature of $M(B)$ in Fig. 3.

The inset of Fig. 4 exhibits the magnetic entropy $S_m(T)$, which was evaluated by integrating the C_m/T data with respect to temperature. Here, the S_m data are vertically offset to reach the value of $R\ln2$ at 5 K for NdCo$_2$Zn$_{20}$ by assuming the full recovery of the magnetic entropy of the doublet ground state. As shown with the arrows, the $S_m(T)$ curves for $y = 1$ and 2 sharply bend at T_N, where S_m are 66% and 80% of $R\ln2$,
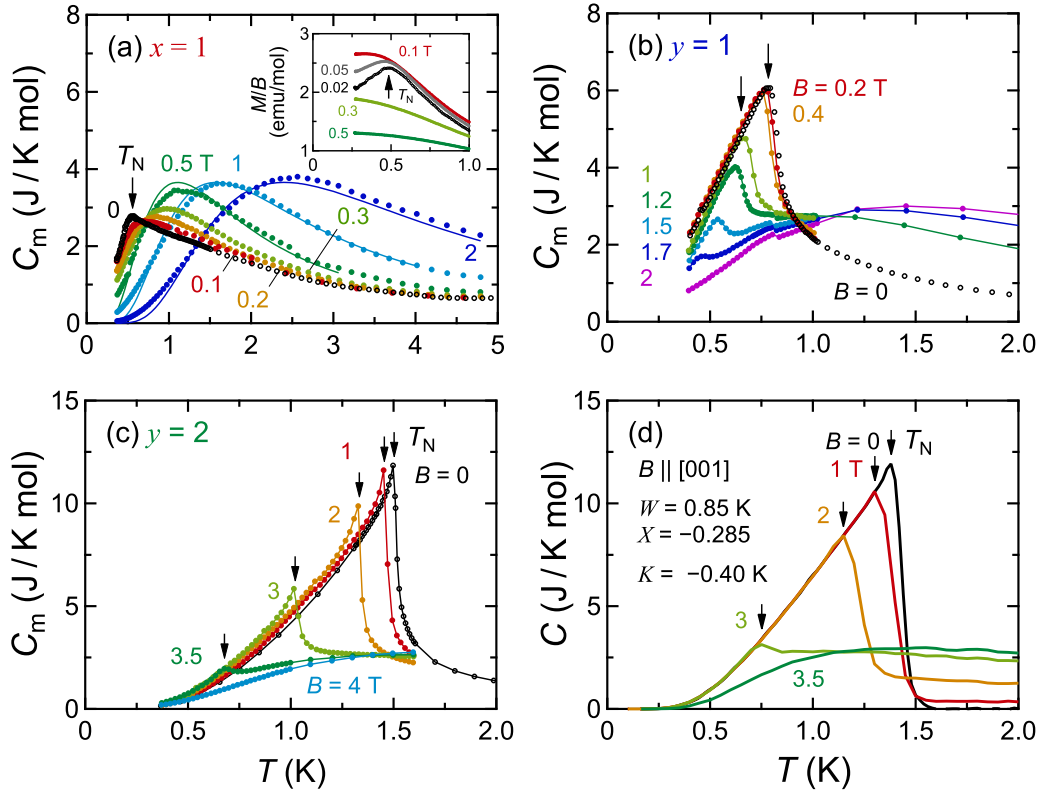
FIG. 5. (a) Magnetic specific heat C_m versus temperature of NdCo$_2$Zn$_{20-x}$Cd$_x$ for $x = 1$. The solid curves for the data in $B = 0.5$, 1, and 2 T are the fits using a two-level model, see text for details. The inset shows the temperature dependence of the magnetization divided by magnetic field, $M(T)/B$, at $B = 0.02$, 0.05, 0.1, 0.3, and 0.5 T. (b,c) $C_m(T)$ of NdCo$_2$Zn$_{20-y}$Ga$_y$ for $y = 1$ and 2, respectively, in magnetic fields. (d) Specific heat evaluated by the mean-field calculation with the CEF parameters of $W = 0.85$ K and $X = -0.285$ [22], and the AFM interaction of $K = -0.40$ K.

respectively. These values are larger than 50% of $R\ln2$ for $y = 0$, indicating suppression of the magnetic fluctuations for $T > T_N$ by the Ga substitution. On the other hand, the S_m data for $x = 1$ continuously decrease on cooling from 5 K through 0.55 K where C_m shows the broad maximum. It is noted that S_m for $x = 1$ at 0.37 K remains as large as 20% of $R\ln2$.

Figures 5(a) to 5(c) show the $C_m(T)$ data of the Cd and Ga substituted samples in magnetic fields. The anomaly of $C_m(T)$ for $x = 1$ shown with the arrow in Fig. 5(a) is not a lambda-type one, but a broad peak at 0.55 K, which resembles the anomaly of $C_m(T)$ with the steep decrease at 1.0 K for NdCo$_2$Zn$_{18}$Sn$_2$ [30]. The inset of Fig. 5(a) shows the temperature variation of the magnetization divided by magnetic field $M(T)/B$, measured at $B = 0.02$, 0.05, 0.1, 0.3, and 0.5 T. The temperature dependence of M/B at $B = 0.02$ T exhibits a maximum at around 0.5 K and then decreases on cooling, which is a characteristic of an AFM order. Thereby, the transition temperature is described as T_N hereafter. With increasing B to 0.1 T, the maximum in the T-dependence of M/B disappears, indicating the collapse of the AFM order. It is noted that the critical magnetic field is much lower than that of 0.32 T for NdCo$_2$Zn$_{20}$ [22].

For $x = 1$, the peak of $C_m(T)$ at $B = 0$ further broadens and shifts to higher temperatures with increasing B up to 2 T. As shown with the solid lines in Fig. 5(a), the maxima for $B \geqslant 0.5$ T can be reproduced as the Schottky specific heat of a singlet-singlet two-level model described by the

equation

$$C = N_A k_B \frac{\Delta^2}{T^2} \frac{\exp(-\Delta/T)}{[1 + \exp(-\Delta/T)]^2}, \qquad (3)$$

where N_A is the Avogadro's number, k_B the Boltzmann constant, and Δ an energy gap. The evaluated values of Δ linearly increase with B, which is expected for the Zeeman splitting of the ground state Γ_6 doublet in the paramagnetic state. Extrapolating the line to $B = 0$ yields $\Delta(B = 0) = 1.7$ K.

On the other hand, as shown in Figs. 5(b) and 5(c), the peak temperatures of C_m for $y = 1$ and 2 go down with increasing B, which is the characteristic behavior of the AFM order. The value of $T_N = 1.5$ K for $y = 2$ is three times higher than $T_N = 0.53$ K for $y = 0$, which is consistent with the development of the AFM interaction by the Ga substitution. Figure 5(d) shows the calculation of the specific heat by adopting the AFM intersite interaction of $K = -0.40$ K and the CEF parameters for $y = 2$ into the mean-field Hamiltonian of Eq. (1). The calculation mostly reproduces the data in Fig. 5(c) not only in zero magnetic field but also in the magnetic fields. Therefore, the AFM order for $y = 2$ is understood by the mean-field model with the intersite AFM interaction. This is reasonable because $S_m(T_N)$ reaches 80% of $R\ln2$ for $y = 2$ as shown in the inset of Fig. 4, suggesting the disappearance of magnetic fluctuations at $T > T_N$.
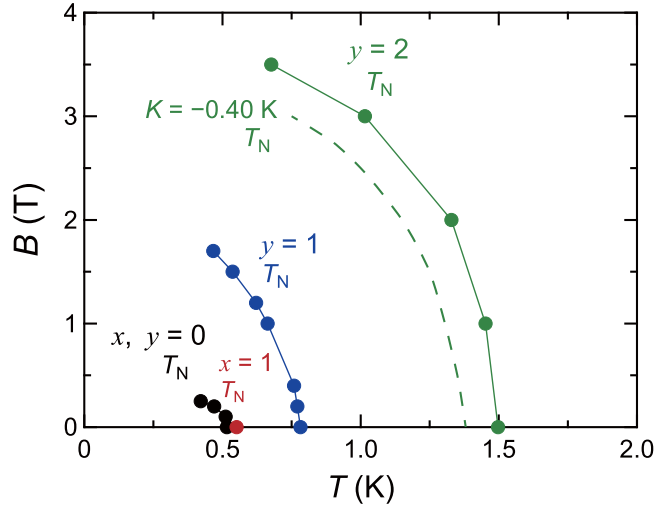
FIG. 6. Magnetic field versus temperature (B–T) phase diagrams of NdCo$_2$Zn$_{20}$ [22] and the Cd and Ga substituted samples. The (green) dashed line indicates the magnetic field variation of T_N for $y = 2$ obtained from the mean-field calculation with the intersite AFM interaction of $K = -0.40$ K.

We show the magnetic field versus temperature (B–T) phase diagrams for $x = 1$, $y = 1$ and 2 constructed from the specific heat measurements, together with the diagram for $x = y = 0$ [22]. As shown in Fig. 6, T_N for $y = 1$ and 2 decreases by the application of the magnetic fields. Since the intersite AFM interaction between the Nd moments is enhanced by the Ga substitution as mentioned above, the area of the AFM ordered phase is successively expanded with increasing the Ga content y from 0 to 2. In addition, the magnetic-field variation of T_N for $y = 2$ can be reproduced by the mean-field calculation with the intersite AFM interaction of $K = -0.40$ K as shown with the (green) dashed line. On the other hand, for the Cd substitution, $T_N = 0.55$ K for $x = 1$ is comparable with $T_N = 0.53$ K for $x = 0$, whereas the magnetic field dependence is quite distinct; the AFM order for $x = 1$ collapses by application of a weak magnetic field of $B = 0.1$ T, which is much lower than the critical magnetic field of 0.32 T for $x = 0$ [22].

Let us discuss how the first-order AFM transition of NdCo$_2$Zn$_{20}$ is modified by the Cd and Ga substitutions. By the Ga substitution with $y = 1$ and 2, the curvature of $M(B)$ is suppressed, indicating the development of AFM interaction between the Nd moments. The development of intersite AFM interaction enhances T_N by three times from 0.53 K for $y = 0$ to 1.5 K for $y = 2$. The AFM order is probably stabilized by the addition of 4p electrons donated from the Ga ion. This doping could modify the Ruderman–Kittel–Kasuya–Yosida (RKKY) interaction between the Nd moments through modulation of the Fermi surface of the conduction electrons. Thereby, the enhanced RKKY interaction favors the second-order AFM transition rather than the first-order one. It should be recalled that the 4p electron doping in the isostructural PrIr$_2$Zn$_{20}$ by substituting Ga for Zn strengthen the c–f hybridization [14], which may enhance the RKKY-type exchange interaction among quadrupole moments. However, the quadrupole order in PrIr$_2$Zn$_{20}$ collapses by the Zn-site substitution, which is attributed to splitting of the non-Kramers

doublet by symmetry lowering of the Pr site due to the local distortion.

Otherwise, symmetry lowering due to the possible structural transition by the Ga substitution may suppress the first-order transition in NdCo$_2$Zn$_{20}$. A theoretical calculation using a four-sublattice bcc Ising model with competing interactions proposed that a first-order transition could be changed to second order if the degeneracy of AFM-ordered states was lifted [43]. In fact, we found that the first-order transition in NdCo$_2$Zn$_{20}$ is changed to the second-order one by application of magnetic fields along the [100] direction [26]. This magnetic-field-induced crossover is probably attributed to the symmetry lowering by the application of the magnetic fields.

In contrast to the Ga substitution, the Cd substitution suppresses the extremely sharp peak of $C_m(T)$ due to the first-order AFM transition to become the broad peak as described above. By the Cd substitution, the magnetic exchange interactions may be disordered, resulting in some distribution of the transition temperatures. If this is the case, the specific heat peak could be broadened to hinder the coherency of the AFM-ordered state. Thereby, the remaining magnetic entropy of 20% of $R\ln 2$ at 0.37 K is probably ascribed to the magnetic fluctuations due to the competitive magnetic interactions inherent in the Nd diamond sublattice. We propose that the competitive interactions can play a role, not only in the first-order AFM transition, but also in enhancing the magnetic fluctuations. Such modification of the ground state by the Zn-site substitution may be relevant to a spin-liquid state due to the magnetic frustration in a Nd pyrochlore lattice with the same space group of $Fd\bar{3}m$ [44,45]. We expect this concept gives a key hint to understand the anomalous transport and magnetic properties often observed in the series of RTr_2X_{20}.

IV. SUMMARY

We measured the electrical resistivity ρ, magnetic susceptibility χ, isothermal magnetization M, and specific heat C of NdCo$_2$Zn$_{20-x}$Cd$_x$ for $x = 1$ and NdCo$_2$Zn$_{20-y}$Ga$_y$ for $y = 1$ and 2. The cubic lattice parameter a for $x = 1$ is 0.38% larger than that of NdCo$_2$Zn$_{20}$, while those of the Ga-substituted samples for $y = 1$ and 2 are hardly changed. The data of the magnetic specific heat $C_m(T)$ for the substituted samples exhibit similar Schottky peaks at around 13 K as in NdCo$_2$Zn$_{20}$, revealing the rigid CEF scheme with the Γ_6 doublet ground states of the Nd^{3+} ion. The $M(B)$ curve for $x = 1$ at 1.8 K is identical to that of $x = 0$. The suppression of the curvature of $M(B)$ with increasing y suggests development of the intersite AFM interaction. The extremely sharp peak of C_m at $T_N = 0.53$ K for $x = 0$ is reduced to a broad peak at 0.55 K by the Cd substitution with $x = 1$. Reduction of the magnetic susceptibility on cooling below 0.5 K indicates occurrence of an AFM order. However, since the specific heat does not exhibit a lambda-type anomaly and the magnetic entropy remains 20% of $R\ln 2$ at the lowest temperature of 0.37 K, the exchange interactions between the Nd moments may be disordered by the Cd substitution. On the other hand, by the Ga substitution with $y = 1$ and 2, the $C_m(T)$ data exhibit the lambda-type anomalies at 0.78 and 1.50 K, respectively. For $y = 2$, T_N is three times higher than that for $y = 0$ and $S_m(T_N)$ reaches 80% of $R\ln 2$. This observation is explained as a result that

the suppression of magnetic fluctuations at $T > T_N$ stabilizes the second-order AFM order. In fact, the $C_m(T)$ data and $T_N(B)$ for $y = 2$ are reproduced by the mean-field calculation including the CEF parameters and the AFM interaction. The stabilization of the AFM order by the Ga substitution results from the enhancement of the AFM interaction by the $4p$ electron doping. Therefore, we propose that the first-order AFM transition and the strong magnetic fluctuations above T_N in NdCo$_2$Zn$_{20}$ are ascribed to the competitive magnetic interactions between the Nd moments inherent in the Nd diamond sublattice. It is necessary to investigate the magnetic structures and the magnetic fluctuations by microscopic techniques such as the neutron scattering and/or nuclear magnetic resonance measurements.

[1] T. Nasch, W. Jeitschko, and U. C. Rodewald, Z. Naturforsch. B **52**, 1023 (1997).

[2] M. S. Torikachvili, S. Jia, E. D. Mun, S. T. Hannahs, R. C. Black, W. K. Neils, D. Martien, S. L. Bud'ko, and P. C. Canfield, Proc. Natl. Acad. Sci. USA **104**, 9960 (2007).

[3] Y. Saiga, K. Matsubayashi, T. Fujiwara, M. Kosaka, S. Katano, M. Hedo, T. Matsumoto, and Y. Uwatoko, J. Phys. Soc. Jpn. **77**, 053710 (2008).

[4] F. Honda, Y. Taga, Y. Hirose, S. Yoshiuchi, T. Tomooka, M. Ohya, J. Sakaguchi, T. Takeuchi, R. Settai, Y. Shimura, T. Sakakibara, I. Sheikin, T. Tanaka, Y. Kubo, and Y. Ōnuki, J. Phys. Soc. Jpn. **83**, 044703 (2014).

[5] T. Onimaru, K. T. Matsumoto, Y. F. Inoue, K. Umeo, Y. Saiga, Y. Matsushita, R. Tamura, K. Nishimoto, I. Isao, T. Suzuki, and T. Takabatake, J. Phys. Soc. Jpn. **79**, 033704 (2010).

[6] T. Onimaru, K. T. Matsumoto, Y. F. Inoue, K. Umeo, T. Sakakibara, Y. Karaki, M. Kubota, and T. Takabatake, Phys. Rev. Lett. **106**, 177001 (2011).

[7] A. Sakai and S. Nakatsuji, J. Phys. Soc. Jpn. **80**, 063701 (2011).

[8] A. Sakai, K. Kuga, and S. Nakatsuji, J. Phys. Soc. Jpn. **81**, 083702 (2012).

[9] M. Tsujimoto, Y. Matsumoto, T. Tomita, A. Sakai, and S. Nakatsuji, Phys. Rev. Lett. **113**, 267001 (2014).

[10] T. Onimaru and H. Kusunose, J. Phys. Soc. Jpn. **85**, 082002 (2016).

[11] T. Onimaru, K. Izawa, K. T. Matsumoto, T. Yoshida, Y. Machida, T. Ikeura, K. Wakiya, K. Umeo, S. Kittaka, K. Araki, T. Sakakibara, and T. Takabatake, Phys. Rev. B **94**, 075134 (2016).

[12] T. Yoshida, Y. Machida, K. Izawa, Y. Shimada, N. Nagasawa, T. Onimaru, T. Takabatake, A. Gourgout, A. Pourret, G. Knebel, and J.-P. Brison, J. Phys. Soc. Jpn. **86**, 044711 (2017).

[13] A. Tsuruta and K. Miyake, J. Phys. Soc. Jpn. **84**, 114714 (2015).

[14] R. J. Yamada, T. Onimaru, K. Uenishi, Y. Yamane, K. Wakiya, K. T. Matsumoto, K. Umeo, and T. Takabatake, J. Phys. Soc. Jpn. **88**, 054704 (2019).

[15] Y. Yamane, T. Onimaru, K. Wakiya, K. T. Matsumoto, K. Umeo, and T. Takabatake, Phys. Rev. Lett. **121**, 077206 (2018).

[16] T. Yanagisawa, H. Hidaka, H. Amitsuka, S. Zherlitsyn, J. Wosnitza, Y. Yamane, and T. Onimaru, Phys. Rev. Lett. **123**, 067201 (2019).

[17] D. L. Cox and A. Zawadowski, Adv. Phys. **47**, 599 (1998).

[18] Y. Isikawa, J. Ejiri, T. Mizushima, and T. Kuwai, J. Phys. Soc. Jpn. **82**, 123708 (2013).

[19] K. Wakiya, K. T. Matsumoto, T. Onimaru, K. Umeo, and T. Takabatake, Phys. Procedia **75**, 511 (2015).

[20] K. Wakiya, T. Onimaru, K. T. Matsumoto, Y. Yamane, N. Nagasawa, K. Umeo, S. Kittaka, T. Sakakibara, Y. Matsushita, and T. Takabatake, J. Phys. Soc. Jpn. **86**, 034707 (2017).

[21] Y. Yamane, R. J. Yamada, T. Onimaru, K. Uenishi, K. Wakiya, K. T. Matsumoto, K. Umeo, and T. Takabatake, J. Phys. Soc. Jpn. **86**, 054708 (2017).

[22] R. Yamamoto, T. Onimaru, R. J. Yamada, Y. Yamane, Y. Shimura, K. Umeo, and T. Takabatake, J. Phys. Soc. Jpn. **88**, 044703 (2019).

[23] T. Namiki, Y. Murata, K. Baba, K. Shimojo, and K. Nishimura, JPS Conf. Proc. **3**, 011055 (2014).

[24] T. Namiki, K. Nosaka, K. Tsuchida, Q. Lei, R. Kanamori, and K. Nishimura, J. Phys.: Conf. Ser. **983**, 012017 (2016).

[25] T. Namiki, Q. Lei, Y. Isikawa, and K. Nishimura, J. Phys. Soc. Jpn. **85**, 073706 (2016).

[26] R. Yamamoto, T. Onimaru, Y. Yamane, A. Wörl, Y. Tokiwa, P. Gegenwart, and T. Takabatake (unpublished).

[27] T. Hotta, J. Phys. Soc. Jpn. **86**, 083704 (2017).

[28] D. Bergman, J. Alicea, E. Gull, S. Trebst, and L. Balents, Nat. Phys. **3**, 487 (2007).

[29] S.-B. Lee and L. Balents, Phys. Rev. B **78**, 144417 (2008).

[30] Y. Isikawa, T. Mizushima, J. Ejiri, S. Kitayama, K. Kumagai, T. Kuwai, P. Bordet, and P. Lejay, J. Phys. Soc. Jpn. **84**, 074707 (2015).

[31] F. Izumi and K. Momma, Solid State Phenom. **130**, 15 (2007).

[32] See Supplementary Material at http://link.aps.org/supplemental/10.1103/PhysRevB.104.155112 for the characterization of synthesized samples and the magnetic susceptibility plotted with χT versus T, which includes Refs. [22,31].

[33] T. Sakakibara, H. Mitamura, T. Tayama, and H. Amitsuka, Jpn. J. Appl. Phys. **33**, 5067 (1994).

[34] T. Onimaru, N. Nagasawa, K. T. Matsumoto, K. Wakiya, K. Umeo, S. Kittaka, T. Sakakibara, Y. Matsushita, and T. Takabatake, Phys. Rev. B **86**, 184426 (2012).

[35] K. Iwasa, H. Kobayashi, T. Onimaru, K. T. Matsumoto, N. Nagasawa, T. Takabatake, S. Ohira-Kawamura, T. Kikuchi, Y. Inamura, and K. Nakajima, J. Phys. Soc. Jpn. **82**, 043707 (2013).

[36] T. Hasegawa, N. Ogita, and M. Udagawa, J. Phys.: Conf. Ser. **391**, 012016 (2012).

[37] K. Asaki, H. Kotegawa, H. Tou, T. Onimaru, K. T. Matsumoto, Y. F. Inoue, and T. Takabatake, J. Phys. Soc. Jpn. **81**, 023711 (2012).

[38] K. Wakiya, T. Onimaru, S. Tsutsui, T. Hasegawa, K. T. Matsumoto, N. Nagasawa, A. Q. R. Baron, N. Ogita, M. Udagawa, and T. Takabatake, Phys. Rev. B **93**, 064105 (2016).

[39] T. Onimaru, K. T. Matsumoto, N. Nagasawa, Y. F. Inoue, K. Umeo, R. Tamura, K. Nishimoto, S. Kittaka, T. Sakakibara, and T. Takabatake, J. Phys.: Condens. Matter **24**, 294207 (2012).

[40] K. Wakiya, T. Onimaru, S. Tsutsui, T. Hasegawa, K. T. Matsumoto, Y. Yamane, N. Nagasawa, A. Q. R. Baron, N.

Ogita, M. Udagawa, and T. Takabatake, J. Phys. Soc. Jpn. **90**, 024602 (2021).

[41] K. R. Lea, M. J. M. Leask, and W. P. Wolf, J. Phys. Chem. Solids **23**, 1381 (1962).

[42] M. Hutchings, Solid State Phys. **16**, 227 (1964).

[43] J. R. Banavar, D. Jasnow, and D. P. Landau, Phys. Rev. B **20**, 3820 (1979).

[44] S. Petit, E. Lhotel, B. Canals, M. C. Hatnean, J. Ollivier, H. Mutka, E. Ressouche, A. R. Wildes, M. R. Lees, and G. Balakrishnan, Nat. Phys. **12**, 746 (2016).

[45] E. Lhotel, S. Petit, S. Guitteny, O. Florea, M. Ciomaga Hatnean, C. Colin, E. Ressouche, M. R. Lees, and G. Balakrishnan, Phys. Rev. Lett. **115**, 197202 (2015).